MEASURING OF RESIDUAL STRESSES IN STRONGLY TEXTURED THIN FILMS

E. Dobročka[1], P. Novák[2], D. Búc[3]

[1]*Institute of Electrical Engineering, Slovak Academy of Sciences, Dúbravská cesta 9,841 04 Bratislava, Slovak Republic*

[2]*Institute of Nuclear and Physical Engineering, Faculty of Electrical Engineering and Information Technology, Slovak University of Technology, Ilkovičova 3, 812 19 Bratislava, Slovak Republic*

[3]*Institute of Electronics and Photonics, Faculty of Electrical Engineering and Information Technology, Slovak University of Technology, Ilkovičova 3, 812 19 Bratislava, Slovak Republic*

edmund.dobrocka@savba.sk

The presence of residual stresses in the near surface region of bulk materials and in thin films is a general problem of various technologies. Among a number of methods developed for stress analysis, X-ray diffraction methods are of special importance due to their capability to analyze the depth variation of the residual stresses. Since the first stress determination by X-ray diffraction in the 1930s a large variety of measuring methods and evaluation procedures were developed. While the standard $\sin^2\psi$ method can be easily used for bulk materials, it is not applicable for thin films, where steep stress gradient perpendicular to the sample surface can be present. In this case the methods based on grazing incidence (GI) set-up are more appropriate. The constant (and usually small) angle of incidence α, that is a characteristic feature of GI X-ray diffraction, ensures that the information depth does not change during the measurement. The GI method of stress determination is classified as multiple $\{hkl\}$ mode in comparison with the $\sin^2\psi$ method, that uses only one set of $\{hkl\}$ planes while the angle of sample inclination ψ varies. The GI method is based on the fact that all diffraction vectors contributing to the GI diffraction pattern make different angles with the surface normal of the sample and provide sufficient set of data for stress evaluation. However, this method of stress measurement fails if the analyzed layer is strongly textured. In this case the orientation of the diffraction vectors is sharply localized and the number of diffractions registered in the measurement performed at constant α and ϕ (usually $\phi = 0$) may be insufficient for the evaluation of the stress state.

In the presented contribution a modified method combining multiple $\{hkl\}$ and multiple ϕ modes of stress measurements is outlined. Measuring at $\phi \neq 0$ can significantly increase the number of accessible diffractions. The analyzed film is supposed to have a fibre texture with the texture axis parallel to the surface normal. The most probable values of angles ψ between the diffraction vectors and the direction are calculated from single crystal data. In order to measure the diffraction with Bragg angle θ at selected angle of incidence α, the tilting angle ψ and the rotation angle ϕ of the goniometer have to be calculated according to relations

$$\cos^2\psi = \frac{\cos^2\theta + 2\cos\theta\sin\alpha\sin\psi - \sin^2\alpha}{\cos^2\alpha}$$

and
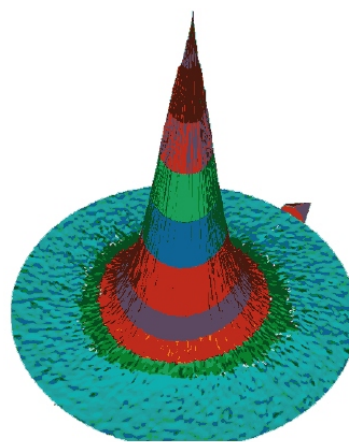
Figure 1. 3D Pole figure 002 of ZnO layer measured within the angular range $\psi = 0° - 30°$.

$$\sin\phi = \frac{\sin\psi}{\cos\alpha}.$$

Due to rotational symmetry of the texture there is no specific restriction for the azimuthal angle ϕ.

The described method was used for evaluation of biaxial stress in ZnO layers deposited on (111) GaP substrates. The stress measurements were performed on as deposited samples and repeated after annealing at 300 °C for 1 hour in N_2 atmosphere. The details of sample preparation are given elsewhere [1]. The layers exhibit strong fibre texture with [001] axis perpendicular to sample surface, the 002 pole figure is shown in Fig. 1. Due to this texture, only three diffractions (002, 103 and 203) with sufficient intensities can be used for stress evaluation, when the diffraction pattern is recorded in standard GI set-up with $\alpha = 1.5°$ and $\phi = 0°$. However, polycrystalline hexagonal ZnO provides 20 diffractions in the range $2\theta < 122°$ (for $Cu K\alpha$ radiation) with relative intensities above 1%, 17 of them are accessible by an appropriate choice of angles ψ and ϕ for a constant angle of incidence $\alpha = 1.5°$. Ten strongest diffractions were measured for different values of ϕ around the ideal angle corresponding to single crystal data.

The results for annealed sample are collected in standard $\sin^2\psi$ plot in Fig. 2. It is seen that the points cover almost uniformly the whole range of the parameter $\sin^2\psi$. The crystallite group method proposed for thin films with fibre texture [2] was employed for the calculation of biaxial stress. The appropriate relation for hexagonal crystals with this type of texture has the form

$$\varepsilon = s_{33}\sigma + [(s_{11}+s_{12}-2s_{13})\sin^2\psi - 2s_{13}]\sigma$$

It was found that the stress in ZnO layers is compressive and its value decreased significantly upon annealing from 3 GPa to 0.5 GPa.

The method enables to analyze also the depth variation of the stress by changing the angle of incidence . However, approaching the critical angle for total external reflection, an appropriate correction of measured diffraction angles has to be made. In addition, for inclined geometry ($\psi \neq 0$) the plane of refraction does not coincide with the diffraction plane and the standard corrections have to be modified [3]. Further improvements can be achieved by applying more sophisticated models developed for thin films [4].

1.   D. Búc, J. Kováč, V. Kutiš, J. Murín, M. Čaplovičová, J. Škriniarová, P. Novák, J. Novák, S. Hasenöhrl, E. Dobročka, In: *Proc. of the jointly organized WCCM XI, ECCM V, ECFD VI*, Eds. E. Oňate et al., Barcelona, CIMNE 2014. ISBN: 978-84-942844-7-2, 2846.
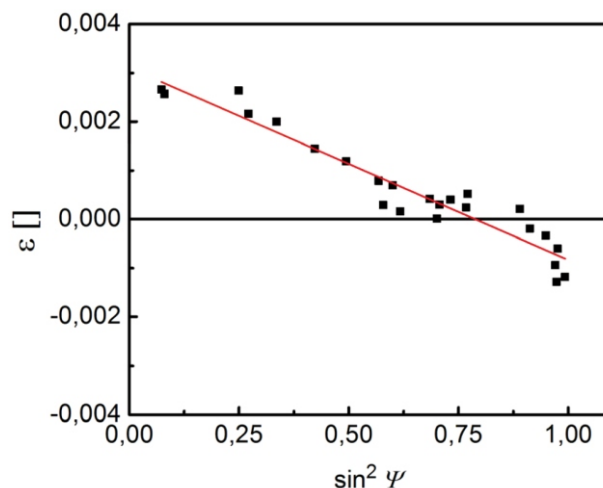
Figure 2. $\sin^2\psi$ plot based on the combination of multiple *hkl* and multiple ψ mode of stress measurement.

2.   V. Hauk, *Structural and Residual Stress Analysis by Non-destructive Methods.* Amsterdam: Elsevier. 1997.

3.   Ch. Genzel, *Mat. Sci. Technol.*, **21**, (2005), 10.

4.   U. Welzel, J. Ligot, P.Lamparter, A. C. Vermuelen, E. J. Mittemeijer, *J. Appl. Cryst.*, **38**, (2005), 1.

L17

X-RAY DIFFRACTION ANALYSIS OF COAL

M. Černík, Z. Kromková, P. Vranec, A. Mašlejová

U.S.Steel Košice, s.r.o., Vstupný areál U.S. Steel, 044 54 Košice
mcernik@sk.uss.com, zkromkova@sk.uss.com, pvranec@sk.uss.com, amaslejova@sk.uss.com

Coal has been used for production of heat and energy for years. Even nowadays energetic industry consumes significant amount of coal for production of electric energy. High amount of coal is also spent during the production of pig iron. U. S. Steel Košice, s.r.o. purchases and combust coal from different suppliers. The quality of such coal is crucial for the combustion process with regard to the ecology. The quality is considered by different petrographic parameters such as carbon, hydrogen and nitrogen content in the inflammable (daf – dry ash free), content of water, minerals, sulfur, volatile substances etc.

The quality and content of minerals in the coal is determined by chemical procedures, however such data can be optimized by X-ray diffraction method. Measurement and evaluation of diffraction patterns of coal was carried out by several authors [1-3], who refined the mineralogical composition of the coal according to the coal deposit. Among the most common occurring minerals in the coal quartz, kaolinite, muscovite, pyrite, carbonates – calcite, dolomite, siderite and oxides – magnetite, hematite are worth to mention. Coal combustion is carried out at high temperatures, where the minerals change their phase composition, melt and release unfavorable gases, such as CO_2 (carbonates) and sulfur (pyrite).

X-ray diffraction analysis was performed on selected samples of black coal. Table 1 summarizes the results of the analyses with the average, minimal and maximum values of determined minerals. Obtained results vary qualitatively and quantitatively according to the sample selection and collection. Graph present in Fig. 1 shows typical diffraction pattern of black coal. Diffraction patterns were measured using Co Ka wavelength and line detector installed on our diffraction device at our X-ray laboratory. Evaluation and refinement was carried out using TOPAS software with Rietveld method.

The importance of measurement and evaluation of diffraction patterns of coal is not just in the analysis of mineralogical composition, but also in the investigation of structural parameters of carbon itself. Pure carbon is graphite with lattice parameters of a = 0.2464 nm and c = 0.6711 nm. Carbon present in coal is not in pure mineralogical form, it is not closely arranged as it contains except of inorganic component also organic part with volatile substances. According to the literature the authors recommend to study the structure of carbon after the removal of mineralogical part in the coal. This needs to be done by leaching of the coal in concentrated acids such as HF and HCl. After the removal of minerals in the coal authors studied only dif-
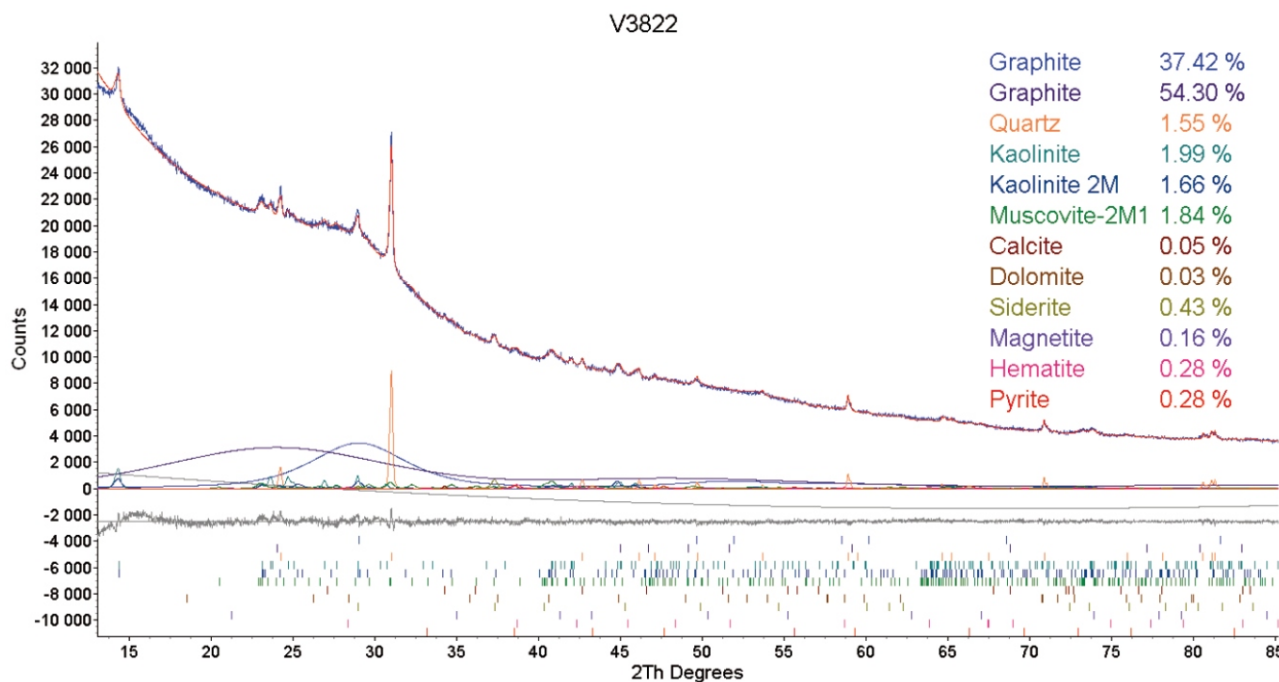
V3822

Graphite	37.42 %
Graphite	54.30 %
Quartz	1.55 %
Kaolinite	1.99 %
Kaolinite 2M	1.66 %
Muscovite-2M1	1.84 %
Calcite	0.05 %
Dolomite	0.03 %
Siderite	0.43 %
Magnetite	0.16 %
Hematite	0.28 %
Pyrite	0.28 %

Figure 1. Detail of the refined diffraction pattern.

fraction profile of the strongest plane (002) of carbon by differentiating on the aliphatic and aromatic part. Aromatic ring stacking is closer the d_{002} value of graphite. Parameter aromaticity f_a, which perfectly correlates with the petrographic parameter C_{daf}, was calculated from the obtained integral values [4, 5].

The aim of our research was to find the structural parameters of carbon directly from the measured diffraction pattern without the leaching of the coal in concentrated acids. For this purpose Rietveld method was used. Diffraction patterns of selected samples of coal were refined in the TOPAS software in the way that the differentiation of the carbon on aliphatic and aromatic part was obtained by defining two structures of carbon, Fig. 1. By this way we were

able to obtain mass portions of aliphatic and aromatic components of carbon in coal with refined lattice parameters, interlayer distance and crystalline size. These parameters perfectly correlate between each other. The graph in Fig. 2 shows the relation of interlayer distance d_{002} on mass portion of carbon. Both trend lines are directed to the amount of 50 % at standard value of $d_{002} = 0.335$ nm what is a perfect coal and thus graphite in the limit.

1   I. Siddigui, M.T. Shah, I. Ahmed: X-Ray Diffraction Analyses of Thar, Sonda and Meting - Jhimpir Coalfields, Sindh; Sind Univ. Res. Jour Vol. 41 (2009) p. 67-74.

2   R. S. Winburn, S. L. Lerach, B.R. Jarabek, M.A. Wisdom, D.G. Grier, G.J. McCarthy: Quantitative XRD Analysis of Coal Combustion By-Product by the Rietveld Method,

IDENTIFIED PHASE COMPOSITION			AVERAGE	MIN	MAX
CHEMICAL FORMULA	MINERALOGICAL NAME	SPACE GROUP	CONTENT [WT %]	CONTENT [WT %]	CONTENT [WT %]
C	Graphite	(166) R-3m	**93.7**	83.9	93.7
SiO_2	Quartz	(152) P3121	**3.1**	0.5	3.1
$Al_2(Si_2O_5)(OH)_4$	Kaolinite 2M	(001) P1	**5.3**	1.4	5.3
$Al_2(Si_2O_5)(OH)_4$	Kaolinite	(001) P1	**2.4**	0.2	2.4
$(K,Na)Al_2(Si,Al)_4O_{10}(OH)_2$	Muscovite 2M1	(015) C12/c1	**4.6**	0.9	4.6
FeS_2	Pyrite	(205) Pa-3	**0.9**	0.1	0.9
$CaCO_3$	Calcite	(167) R-3c	**1.5**	0	1.5
$MgCaCO_3$	Dolomite	(148) R-3	**2.2**	0	2.2
$FeCO_3$	Siderite	(167) R-3c	**1.1**	0	1.1
Fe_3O_4	Magnetite	(227) Fd-3m	**2.4**	0.1	2.4
Fe_2O_3	Hematite	(167) R-3c	**0.4**	0	0.4

Table 1. General phase composition of the analyzed coal samples.

JCPDS Internation Centre for Diffraction Dta 2000, Advances in X-ray Analysis, Vol. 42, p. 387-396.

3   C.R. ward, D.French: Relatin between Coal and Fly Ash Mineralogy, Based on Qualitative X-ray Diffraction Methods, World of Coal Ash (WOCA), April 11-15, 2005, Lexington, Kentucky, USA.

4   B. Mamoj, A.G. Kunjomana: Study of Stacking Structure of Amorphous Carbon by X-ray Diffraction Technique; Int. J. Electrochem. Sci. 7 (2012) p. 3127-3134.

5   P. Boral, A.K. Varma, S. Maity: X-Ray Diffraction Studies of Some Structurally Modified Indian Coal and Their Correlation with Petrographic Parameters; Current Science, Vol. 108, No. 3, (2015) p. 384-394.
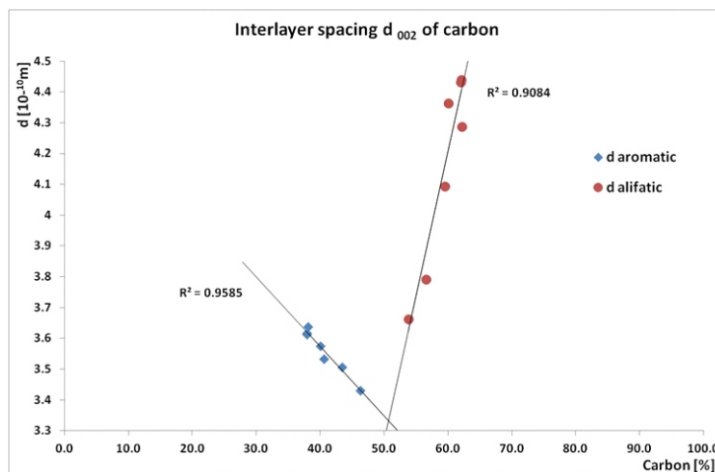
Figure 2. Interlayer $d_{aromatic}$ and $d_{aliphatic}$ vs. carbon content of coal.

L18

SHAPE MEMORY ALLOYS INVESTIGATED BY EBSD METHOD

J. Kopeček, L. Klimša, J. Remiášová, V. Kopecký, M. Vronka, O. Heczko

Fyzikální ústav AV ČR, v. v. i.,, Na Slovance 2, 182 21 Praha 8, Praha 8

The shape memory alloys (SMAs) have been used since 1971. The main attention turned from the first applied alloy Nitinol to copper-based alloys, but the second half of 80's returned the leading position in the field to Nitinol as a stent implants material. The significant boost for SMAs was the discovery of the magnetically induced martensitic transformation in Ni_2MnGa based alloys. Nevertheless, the field of SMA is much wider and contain various, even peculiar, alloys connected just by presence of the martensitic transformation - diffusionless transformation, where atoms moves just the distances shorter than lattice parameter. Compared to usual habit of metals, the response to mechanical stress (or other external force) in SMAs is not standard, and there should be an explanation, why the deformation is not proceeded via creation of dislocations. The processes behind such behavior are usually the long distance forces of precipitates and the high or specific density of the planar defects in lattice.

In the presented paper we overview of the fruitful exploration of the electron back-scattered diffraction (EBSD) method to investigate the solid state phase transformations in SMAs. EBSD method, as the improvement and evaluation of observed Kikuchi lines, is even older than electron microscopy itself and dates back to 1928. It allows us to establish the orientation of the known lattice in the point illuminated by the electron beam. Presented results cover the wide range of SMAs.

The transformation in Co-Ni-Al alloys is the example of the stress induced martensitic transformation stabilized by the particles of the non-transforming phase. The real martensitic variants were distinguished from polishing artefacts having the same shape as these variants by EBSD.

The extremely similar variants of very slightly monoclinic martensitic phases in Ni-Mn-Ga alloys can be distinguished by EBSD too, although some differences are below the resolution limits of the method and evaluation must be improved by manual evaluation or additional presumptions. The more known SMA alloys in the same category represents NiTi being functionalized by precipitates and copper based alloys as Cu-Al-Ni driven by a cascade of martensitic transformations and their twinning boundaries.

L19

MIKROSTRUKTURA TAŽENÉ PERLITICKÉ OCELI A JEJÍ OBRAZ V RTG. DIFRAKCI

Daniel Šimek[1], Anja Oswald[2], Rosita Schmidtchen[2], David Rafaja[2]

[1]*Institute of Physics, Academy of Sciences of the Czehc Republic, Na Slovance 2, Praha 8*
[2]*Bergakademie - Technical University Freiberg, Germany*

Perlitická ocel C80D (0,80 hm.% uhlíku) připravená válcováním s různými rychlostmi chlazení a následně tažená za studena za pomoci raznic různých geometrií vykazuje odlišné mechanické vlastnosti (pevnost, tažnost). Byla zkoumána souvislost s mikrosktrukturou zobrazenou pomocí metalografie a řádkové elektronové mikroskopie (SEM), která vykazuje známé empirické tendence (mezilamelární vzdálenost v perlitu, uspořádávání lamel) a dále souvislost mikrostruktury s veličinami pozorovatelnými v rtg. difrakci (XRD). Pevnost válcoaných perlitických ocelí pak vykazuje souvislost s hustotou lamel (SEM) a mikronapětím (XRD) pocházejícím od misfit-dislokací na rozhraní ferrit-cementit, zatímco nárůst pevnosti při studené deformaci vykazuje souvislost reorientací lamel, kterou lze pozorovat ve vývoji krystalografické textury. Měřením rtg. difrakce tak lze popsat mikrostrukturní stav jak válcovaných tak tažených vzorků a odhadnout jejich mechanické vlastnosti, případně další zpracovatelnost materiálu.

L20

LASEROVÉ OPRACOVÁNÍ MATERIÁLŮ

M. Čerňanský

Fyzikální ústav AV ČR, v. v. i., Na Slovance 2, 182 21 Praha 8, Česká republika
cernan@fzu.cz

Důsledkem prostorové a časové koherence laserového záření je koncentrace výkonu, resp. energie, kterou lze optickými soustavami získat. Čočkou nebo soustavou zrcadel lze laserový svazek v jejich ohnisku fokusovat na průměr blížící se vlnové délce. Velmi vysoké hustoty výkonu, které laser může vytvořit jsou ekvivalentní tepelným zdrojům s teplotou nad 20000° C. To umožňuje řezat ocelové desky až 20 mm tlusté kontinuálním laserem CO_2 s výkonem 6 kW při rychlosti 1 m za minutu, nebo vrtání děr a také laserové svařování běžné oceli až do tlouš ky 12 mm. U laserového svařování ocelí jsou zbytkové deformace 3 až 5 krát menší než u obloukového svařování. Charakteristické je zmenšení šířky zóny plastických deformací ve srovnání s obloukovým svařováním, což vede k významnému snížení pnutí. Laserové svařování lze tak považovat za přesnou výrobní operaci, která může být považována za konečnou a nepotřebuje následné odstranění zbytkových deformací nebo mechanického opracování svárů.

Uvedené aplikace laseru – vrtání, řezání a svařování - představují objemové procesy. Velmi atraktivní jsou však procesy úpravy povrchů, které mohou být bez natavení povrchu, jako je žíhání a kalení, resp. transformační vytvrzování. S natavením povrchu se provádí povrchové legování, opatřování povlaky (povlakování), zpevňování povrchu disperzními částicemi, zjemňování zrna, amorfizace a kalení z kapalného stavu. S natavením povrchu se také provádí zpracování šoky, resp. rázy, spočívajícími v tlakovém účinku vypařeného plynného media nad povrchem kovu. Působením krátkých pulsů s vysokou hustotou energie vznikají v povrchové vrstvě materiálu tlaková zbytková pnutí, které významně zlepšují zejména únavové vlastnosti materiálu tím, že omezují vznik a rozvoj povrchových trhlin.

Optický ohřev laserem je bezkontaktní. Do ohřívaného materiálu se nedostávají žádné nečistoty ani nežádoucí příměsi. Může se provádět ve vakuu nebo v inertní atmosféře. Pomocí vhodných optických prvků je proveditelný i v místech nedostupných pro jiné způsoby ohřevu. Fokusací záření laseru je možné jeho účinek omezit na velmi malou plochu a také omezit na výjimečně krátkou dobu. Tím lze v prostoru vymezit jeho tepelné účinky, zejména jen na malou hloubku pod povrchem. Pomocí optických soustav lze také svazek laseru vymezit na plochu s požadovanou velikostí nebo ho rozdělit na několik svazků a ty přivádět na různá místa. Mechanickými prostředky je možné zařídit vzájemný pohyb laserového svazku a opracovávaného povrchu.

Účinek laseru lze při optickém ohřevu velmi jemně a velmi přesně dávkovat. Posloupnost jednotlivých operací lze relativně snadno naprogramovat a celý cyklus zautomatizovat. To je podstatné pro hromadnou sériovou výrobu, kde výjimečná reprodukovatelnost podstatně snižuje zmetkovitost. Podle toho jakou strukturu povrchu, resp. jaké vlastnosti povrchu požadujeme, je možné zvolit režim opracování, t. j. zejména hustotu výkonu, dobu působení laserového záření na povrch a dobu relaxace. Tím lze naprogramovat účinek laseru a dosáhnout tak zcela určitého způsobu opracování povrchu.

Ideální konstrukční materiál by měl mít velkou houževnatost při velké povrchové tvrdosti. Houževnatosti se dosahuje popouštěním, tedy pomalým ochlazováním po ohřevu, tvrdosti naopak rychlým ochlazením. Při klasickém kalení s rychlým ochlazením však bohužel roste křehkost jádra materiálu, a proto je použití laseru ke zvýšení tvrdosti povrchu velmi výhodné. Laserovým svazkem se zakalí jen tenká povrchová vrstva bez prohřátí a změn vlastností jádra materiálu, které si ponechá svou houževnatost. Podstatným rozdílem laserového kalení od klasického je to, že laserové kalení může probíhat i s natavením povrchu. Při laserovém kalení bez natavení povrchu probíhají strukturně-fázové transformace v pevném stavu, t.j. transformační vytvrzování. Výhodou laserového opracování je, že umožňuje vytvořit amorfní strukturu přímo na povrchu masivních součástí z kovových

slitin. Bylo však zjištěno, že při laserové amorfizaci povrchu jsou nutné vyšší ochlazovací rychlosti než při dosavadním ochlazování mezi rotujícími válci.

L21

X-RAY DIFFRACTION STUDY OF THE (MAGNETO-)STRUCTURAL TRANSITION IN FeRh THIN LAYERS

L. Horák

Faculty of Mathematics and Physics, Charles University in Prague, Ke Karlovu 5, 121 16 Praha 2
horak@karlov.mff.cuni.cz

The $Fe_{50}Rh_{50}$ material exhibits a reversible magneto-structural transition between a room-temperature antiferromagnetic (AFM) and a high-temperature ferromagnetic (FM) phase approximately at 350 K [1]. At room temperature, the magnetic moment located at the Fe atoms are AFM ordered while there are no localized magnetic moments at the Rh atoms [2]. After the transition, the lattice is discretely expanded and there are localized magnetic moment FM ordered at the Fe atoms, and at the Rh atoms as well [2].

However, the principally first-order transition itself displays continuous behaviour with the presence of the structurally transited but non-magnetic phase [3]. Moreover, the transition shows the temperature/field hysteresis in the lattice parameter and in the magnetic net moment [4].

Most probably, the initial growth of the ferromagnetic phase is stimulated by the defects located at the surface and/or the interface with the substrate [4]. Further, in the thin FeRh layers, the presence of the stable residual FM volume is being observed [5]. It was shown that this volume can be located at the layer/substrate or layer/capping interface [5]. Such defected interfaces can be rich of seeds for the formation of ferromagnetic FeRh regions.

Using High-Resolution X-ray diffractometry (HR-XRD), we have measured several samples of FeRh thin layers with various thicknesses. Benefiting from the different lattice parameter of the AFM and the FM phase, we determined from the measured peak-intensity the volume of both phases in the samples. From the temperature dependent measurement (heating and cooling), we reconstructed the hysteresis loop of the FM/AFM volume (figure 1).

At room temperature, the measured curves were evidently asymmetric indicating the presence of the strong AFM-phase peak and the weak FM-phase peak (see figure 2). We were looking for a rich-Fe interfacial layer that could be a source of that residual FM phase. From the X-ray reflectivity, it follows that our FeRh thin layers themselves can be described by a model of a single homogeneous layer as the measured X-ray reflectivity was successfully fitted by this model. The reflectivity proved that there is no observable FeRh sub-layer with different stoichiometry at the interface with the substrate and/or with the capping layer.

On the other hand, the thickness oscillations were present in the diffraction curves for all temperatures. Their frequency corresponded very well to the thickness obtained from the X-ray. Surprisingly, the width of the possible FM-phase peak was as the same as its width above the transition temperature. Later analysis, when we simulated and

fitted measured curves (figure 2), supported the suspicion that the residual FM volume (although very small) has in the out-of-plane direction the dimension being equal to the film thickness, i.e., it is grown from the very bottom to the
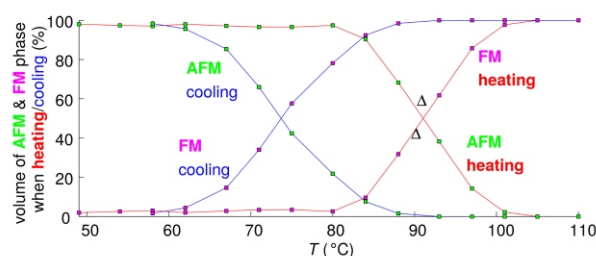
Figure 1. Evolution of the AFM and FM volume during the heating&cooling loop.
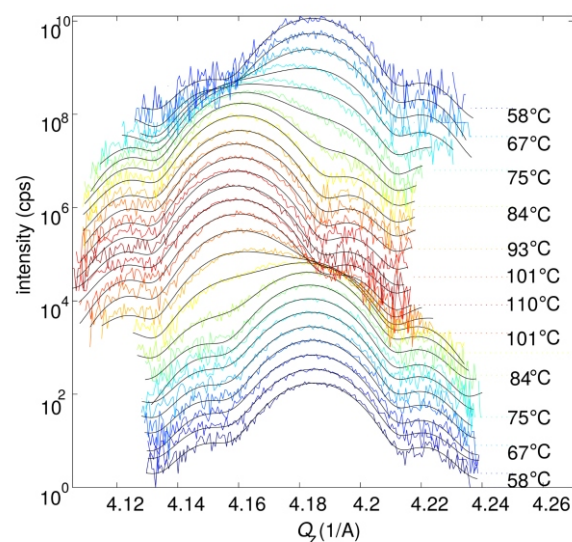
Figure 2. Measured diffraction curves for different temperatures (heating and cooling loop). The experimental data (coloured) are fitted with the simulation (black solid curve).

top of the thin layer.

Besides the findings that the residual ferromagnetic volume can be concentrated at the layer/substrate (or cap) interface [5], we found in our samples that this volume can be laterally spread in the layer in a form of thin columns, but already having their final thickness. Just these columns

could be the seeds for the emerging FM phase during the heating.

1. Zakharov, A. (1964). *Soviet Physics JETP*, 46(6), 2003–2010.

2. Moruzzi, V. L., Marcus, P. M. (1992). *Physical Review B*, **46** (5), 2864–2873.

3. Choi, Y., Keavney, D., Holt, M., and Uhlíř, V. (2014). *arXiv* Preprint.

4. Lu, W., Huang, P., Chen, Z., He, C., Wang, Y., & Yan, B. (2012). *Journal of Physics D: Applied Physics*, **45**, 435001.

5. Baldasseroni, C., Pálsson, G. K., Bordel, C., Valencia, S., Unal, a. a., Kronast, F., ... Hellman, F. (2014). *Journal of Applied Physics*, **115**, 043919.

L22

STRUCTURAL CHARACTERIZATION OF METAL OXIDE BASED GAS SENSOR HETEROSTRUCTURES

T. Roch, T. Plecenik, P. Durina, B. Grancic, M. Mikula, M. Truchly, M. Gregor, L. Satrapinskyy, O. Krsko, A. Plecenik, P. Kus

Department of Experimental Physics, Faculty of Mathematics Physics and Informatics, Comenius University in Bratislava, Mlynska Dolina, 842 48 Bratislava, Slovakia
roch@fmph.uniba.sk

In recent years titanium dioxide (TiO_2) is very intensively studied due to its physical and chemical properties beneficial for many applications, for example in semiconductor metal oxide gas sensing devices. Upon exposure of TiO_2 surface to traces of hydrogen, carbon monoxide, methane or other reducing gases, its resistivity changes dramatically [1]. Sensor response is defined as $S=R_{air}/R_{gas}$, where R_{air} and R_{gas} are resistances measured in air without detected gas and in mixture of air and measured gas, respectively. Typically the contact metallic structures are prepared on top of the TiO_2 film. Oxide layers are deposited on unheated sapphire substrates by reactive DC magnetron sputtering. Platinum contact layers are sputtered on top of the oxide layer. We studied the possibility to utilize stable rutile phase thin films deposited at relatively low temperature on c-cut sapphire substrates. Technological conditions have been chosen in order to obtain highly oriented TiO_2 rutile thin films. Surface topography has been characterized by atomic force microscopy. Structure, texture and the strain evolution has been investigated using X-ray diffraction measurements. Thin films showed epitaxial relationship with respect to the substrate: rutile-TiO_2(100)[001] || Al_2O_3(0001)[100]. Subsequent ex-situ annealing in temperature range from 500 °C to 800 °C leads to increase of crystallite size and improvement of in-plane preferential orientation. The response of samples to hydrogen is decreasing with increasing grain size. We have shown that the stable rutile-TiO_2 thin films can be suitable long-term alternative to metastable anatase TiO_2 sensing material [2].

However we have also proposed promising devices with combined vertically stacked bottom and top contacts of gas-sensing TiO_2 layer [3]. Within sufficiently thin oxide layer the electrons in strong electric field between electrodes get hot. This effect leads to strong increase of sensitivity, shorter dynamical response and possible decrease of operating temperature down to room temperature. If ohmic contact is desired at the metal/TiO_2 interface, the structures has to be subsequently annealed. In order to understand the sensing mechanisms and structural behaviour of such structures upon thermal processing we had to investigate in detail structural properties of such heterostructures [4]. X-ray diffraction, reflectivity, texture and non-ambient temperature measurements has been performed on reference samples of the bilayers TiO_2/Pt and trilayers Pt/TiO_2/Pt. Ex-situ annealing at the temperature of 600 °C for 1 hour leads to increase of crystallite size and improvement of in-plane preferential orientation of Pt interlayer grown on (0001)-oriented Al_2O_3 substrate. Inner 30nm thin layer shows randomly oriented both TiO_2-rutile (R) and anatase (A) phases with the volumetric ratio of R/A ~ 2.6 and with the crystallite size of ~9 nm and ~18 nm, respectively. These data were important input to simulations of electron transport model, which has fit very well to measured resistance data [4].

1. D. E. Williams, *Sens. Actuators B* **57** (1999), 1.

2. A. Haidry, P. Schlosser, P. Durina, M. Mikula, M. Tomasek, T. Plecenik, T. Roch, A. Pidik, M. Stefecka, J. Noskovic, M. Zahoran, P. Kus, A. Plecenik, *Cent. Eur. J. Phys.* **9** (2011), 1351.

3. T. Plecenik, M. Mosko, A. A. Haidry, P. Durina, M. Truchly, B. Grancic, M. Gregor, T. Roch, L. Satrapinskyy, A. Moskova, M. Mikula, P. Kus, A. Plecenik, *Sensors and Actuators B-Chemical* **207**, Part A**,** (2015), 351.

4. T. Roch, P.Durina, B. Grancic, M. Gregor, T. Plecenik, M. Truchly, M. Mikula, L. Satrapinskyy, P. Kus, A. Plecenik, *Appl. Surf. Sci.*, **312**, (2014), 192.

L23

The study of preparation of SrAl$_{12}$O$_{19}$ thin films

R. Uhrecký[1], J. Buršík[1], R. Kužel[2]

[1]*Institute of Inorganic Chemistry of the AS CR, v.v.i., Husinec-Řež č.p. 1001, CZ-25068 Řež*
[2]*Charles University in Prague, Faculty of Mathematics and Physics, Ke Karlovu 5, 121 16 Praha 2*
uhrecky@iic.cas.cz

Hexagonal ferrites thin films based on iron (III) oxides have attracted great interest in the field of magnetic oxide materials. They are used as information storage medium and in diverse microwave applications. In order to improve their functional properties through improved crystallographic and magnetic anisotropy, buffer layers that match structural and chemical properties of ferrite film and substrate materials are frequently used in the growth technology. Hexagonal aluminate with formula SrAl$_{12}$O$_{19}$ is suitable material as buffer layer due to its chemical stability and low lattice misfits parameters against Al$_2$O$_3$ substrate and magnetic hexagonal ferrites.

In our work we studied preparation of a non-magnetic SrAl$_{12}$O$_{19}$ thin film prepared by chemical solution deposition CSD method on Al$_2$O$_3$ (0001) substrate. SrAl$_{12}$O$_{19}$ thin films were prepared in two different ways, i.e. (a) by direct deposition of SrAl$_{12}$O$_{19}$ sol on Al$_2$O$_3$ (0001) substrate, or

(b) in situ reaction of SrO sols with Al$_2$O$_3$ substrate. Prepared films were studied by XRD diffraction and by AFM measurements.

Both approaches lead to the formation of highly oriented 000l SrAl$_{12}$O$_{19}$ thin films. Detailed XRD studies of films show significant differences between both processes. Direct deposition of SrAl$_{12}$O$_{19}$ sols lead to the dense film with hexagonal structure. According XRD analysis, these structures show several in-plane orientation variants.

Layers prepared by solid state reaction between SrO with Al$_2$O$_3$ substrate show only one in-plane orientation of SrAl$_{12}$O$_{19}$. The final film contains sparse columnar hexagonal islands and these islands contain probably different Sr-Al-O phases or unreacted SrO at lower temperatures.
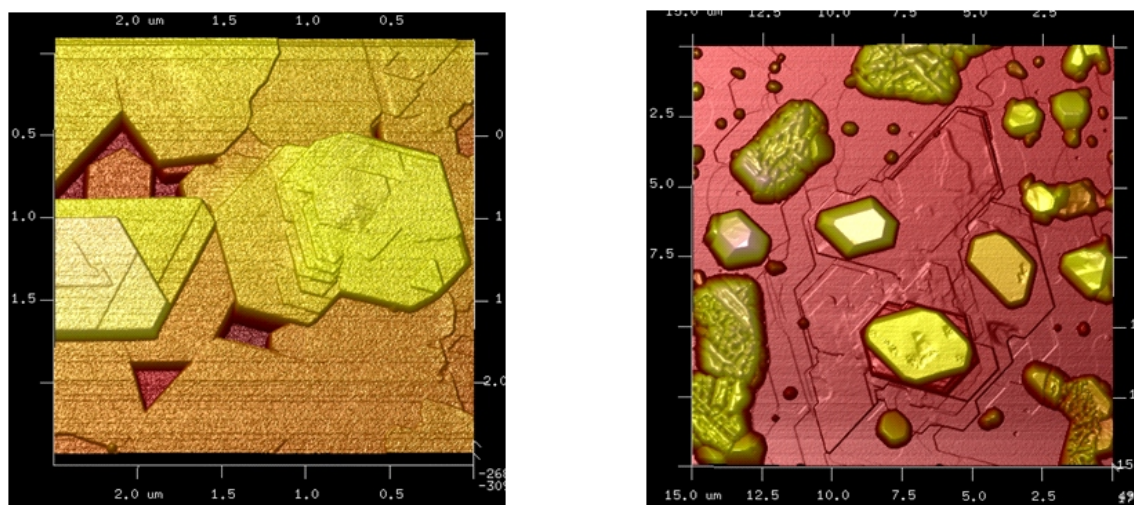
Figure 1. AFM pictures of SrAl$_{12}$O$_{19}$ prepared by direct deposition (left) and by solid state reaction between SrO and Al$_2$O$_3$ (right).

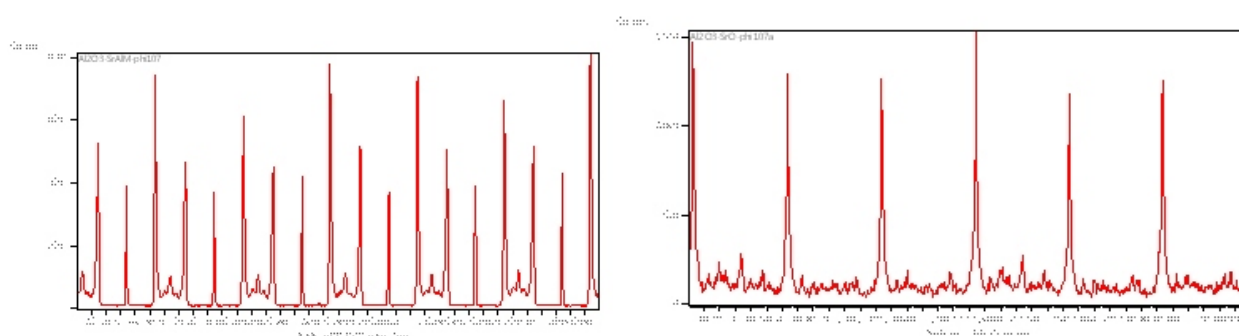**Figure 2**.   scans measured on Al$_2$O$_3$(001)//SrAl$_{12}$O$_{19}$ films prepared by direct deposition (left) and by solid state reaction between SrO and Al$_2$O$_3$ (right).

L24

DETERMINATION OF PHASE COMPOSITION OF IRON SINTERS BY METHODS OF X-RAY DIFFRACTION

P. Vranec, M. Černík, A. Mašlejová

U. S. Steel Košice, s.r.o., Vstupný areál U. S. Steel, 044 54 Košice
pvranec@sk.uss.com, mcernik@sk.uss.com, amaslejova@sk.uss.com

The production of most pig iron is based on the use of iron sinter which consists of various mineral phases formed during the sintering process of iron ore, fluxes and coke ash. Chemical reactions at high temperatures take place during the sintering process. Particles of iron ore and flux interact with each other to form a sinter cake, which consist of iron ore, silico-ferrites of calcium and aluminium (SFCA, Silico-Ferrite of Calcium and Aluminium) [1, 2], dicalcium silicate and amorphous phase. The results of studies by Scarlett et al. [3] indicate that the iron sinter structure is formed by the following phases: iron oxides (ca. 40 – 70 vol%), ferrites (mainly SFCA, ca. 20 %), calcium silicates (up to ca. 10 %) and amorphous phase (up to ca. 10 %). Iron sinters can occasionally contain also phases such as sulphides (FeS), pyroxenes ($(Mg,Fe)SiO_3$), quartz and lime. Summary of common mineral phases occurring in the iron sinters is given in Table 1.

Iron oxides are present in the iron sinters as a residues of non-reacted iron ores or as products crystallizing from the melt. The most common are hematite and magnetite; the presence of wüstite is observed only in the case of iron sinters produced with increased amount of fuel. Calcium ferrites are secondary phases which are formed by a reaction between Fe_2O_3 and CaO, which comes from the additives. The most common are dicalciumferrite ($Ca_2Fe_2O_5$) and monocalciumferrite ($CaFe_2O_4$). Ferrites of complex composition (SFCA) are however highly represented in the

iron sinters. Based on the high mutual chemical affinity of lime and SiO_2, the presence of larnite (Ca_2SiO_4), as well as hedenbergite ($CaFeSi_2O_6$) and pseudowollastonite ($CaSiO_3$) is also observed, which are however ineligible mineral phases due to their acidity. Dominant component of the amorphous phase in iron sinters is mainly SiO_2.

In U. S. Steel Košice, s.r.o. the production of pig iron is also based on the use of iron sinter prepared at four sintering bands. Identification of phase composition of the industrial iron sinters plays a key role in optimization of the sintering process, as well as appropriate selection of the used raw materials. Therefore, the laboratory of X-ray diffraction at the Department of Metallography and Failure Analysis (MaFA) deals with the determination of the phase composition of iron sinters as well. Since the 2005 more than 400 samples have been measured and evaluated at the MaFA.

Diffraction patterns of iron sinters were measured on Bragg-Brentano goniometer equipped with line detector, which significantly shorten the measurement time. For better resolution of the diffraction pattern the Co K radiation with the voltage of 40 kV and current of 35 mA was used. Evaluation of the phase composition was carried out in TOPAS software from Bruker Company. The key factor at evaluation of phase composition from the measured diffraction patterns was the availability of the structure data, where until recently the diffraction patterns were evaluated
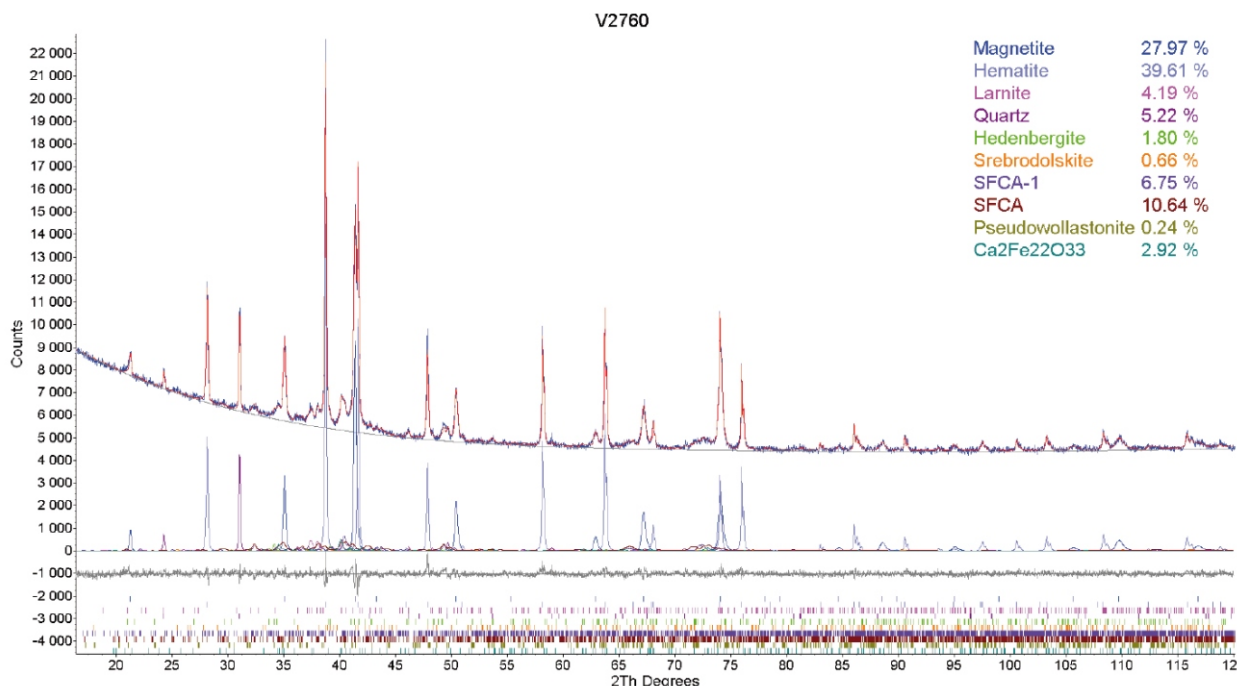

Figure 1. Sample 1, detail of the refined diffraction pattern.

Table 1. Properties of common phases present in iron sinters.

GROUP	MINERAL PHASE	RATIONAL FORMULA	STECHIOMETRIC FORMULA	LATTICE TYPE
Iron oxides	Hematite	α-Fe$_2$O$_3$	α-Fe$_2$O$_3$	Trigonal
	Magnetite	FeO·Fe$_2$O$_3$	Fe$_3$O$_4$	Cubic
Calcium ferrites	Calcium ferrite	CaO·Fe$_2$O$_3$	CaFe$_2$O$_4$	Orthorhombic
	Calcium diferrite	CaO·2Fe$_2$O$_3$	CaFe$_4$O$_7$	Monoclinic
	Dicalcium ferrite	2CaO·Fe$_2$O$_3$	Ca$_2$Fe$_2$O$_5$	Orthorhombic
	Brownmillerite	2CaO·Al$_2$O$_3$·Fe$_2$O$_3$	Ca$_2$(Al,Fe)$_2$O$_5$	Orthorhombic
	SFCA	*	*	Triclinic
Silicates	Larnite	β-2CaO·SiO$_2$	β-Ca$_2$SiO$_4$	Monoclinic
	Hedenbergite	CaO·FeO·2SiO$_2$	CaFeSi$_2$O$_6$	Monoclinic
	Pseudowollastonite	CaO·SiO$_2$	CaSiO$_3$	Monoclinic

* Due to the variable composition, no official formula is accepted

without the presence of SFCA phases. These were replaced by other phases of similar composition, i.e. Ca$_4$Fe$_9$O$_{17}$, CaFe$_5$O$_7$, Ca$_2$Fe$_{22}$O$_{33}$, CaAl$_4$O$_7$ (Grossite), Na(AlSi$_3$O$_8$) (Albite) and others. Recently, the analyses of iron sinters include all available and necessary structure data, what increase the quality of the evaluation. Evaluated diffraction pattern of typical industrial iron sinter is given in Fig. 1 and general phase composition of the analyzed samples of iron sinters together with minimal, maximum and average content of each mineral phase is summarized in Table 2.

1   J.D.G. Hamilton, B.F. Hoskins, W.G. Mumme, W.E. Borbidge, M.A. Montague: The crystal structure and crystal chemistry of Ca$_{2.3}$Mg$_{0.8}$Al$_{1.5}$Si$_{1.1}$Fe$_{8.3}$O$_{20}$ (SFCA): solid solution limits and selected phase relationship of SFCA in the SiO$_2$–Fe$_2$O$_3$–CaO(–Al$_2$O$_3$) system, Neues Jahrbuch für Mineralogie, 161, 1-26 (1989).

2   W.G. Mumme, J.M.F. Clout, R.W. Gable: The crystal structure of SFCA-I, Ca$_{3.18}$Fe$^{3+}_{14.66}$Al$_{1.34}$Fe$^{2+}_{0.82}$O$_{28}$, a homologue of the aenigmatite structure type, and new crystal structure refinements of -CFF, Ca$_{2.99}$Fe$^{3+}_{14.30}$Fe$^{2+}_{0.55}$O$_{25}$ and Mg-free SFCA, Ca$_{2.45}$Fe$^{3+}_{9.04}$Al$_{1.74}$Fe$^{2+}_{0.16}$Si$_{0.6}$O$_{20}$, Neues Jahrbuch für Mineralogie, 173, 93-117 (1998).

3   N.V.Y. Scarlett, M.I. Pownceby, I.C. Madsen, A.N. Christensen: Reaction sequences in the formation of silico-ferrites of calcium and aluminum in iron ore sinter, Metallurgical and materials transactions B, 35B, 929-936 (2004).

Table 2. General phase composition of the analyzed iron sinter samples.

IDENTIFIED PHASE COMPOSITION			MIN	MAX	AVERAGE
CHEMICAL FORMULA	MINERALOGICAL NAME	SPACE GROUP	CONTENT [WT%]	CONTENT [WT%]	CONTENT [WT%]
Fe$_3$O$_4$	Magnetite	(227) Fd-3m	14.5	46.6	**28.9**
Fe$_2$O$_3$	Hematite	(167) R-3c	10.2	56.3	**32.5**
CaSiO$_4$	Larnite	(014) $P2_1$/c	2.5	8.3	**5.6**
SiO$_2$	Quartz	(152) $P3_1$21	2.7	7.8	**4.7**
CaFeSi$_2$O$_6$	Hedenbergite	(015) $C2$/c	1.4	4.7	**2.8**
Ca$_2$Fe$_2$O$_5$	Srebrodolskite	(062) $Pnma$	0.2	4.0	**0.8**
Ca$_{2.45}$Fe$_{9.04}$Al$_{1.74}$Fe$_{0.16}$Si$_{0.6}$O$_{20}$	SFCA	(002) P-1	6.1	19.7	**11.9**
Ca$_{3.18}$Fe$_{14.66}$Al$_{1.34}$Fe$_{0.82}$O$_{28}$	SFCA-I	(002) P-1	1.7	20.7	**10.2**
CaSiO$_3$	Pseudowollastonite	(002) P-1	0.1	0.8	**0.4**
Ca$_2$Fe$_{22}$O$_{33}$	Calcium Iron Oxide	(155) R32	0.0	4.4	**2.3**